Chinese Chemical Letters 37 (2026) 111651

Contents lists available at ScienceDirect

Chinese Chemical Letters

journal homepage: www.elsevier.com/locate/cclet

Functional group-engineered crosslinking for high-performance sodium storage of biomass-derived hard carbon

Yandong Xie[a], Sishi Li[a], Shiyin Xie[a], Yulong Zhang[b], Ziqiang Fan[a], Yuecong Chen[a], Jian Zhu[a], Qingyun Dou[a], Xingbin Yan[a,*]

[a] Department of Materials Science and Engineering, Sun Yat-sen University, Guangzhou 510275, China
[b] School of Physics and Optoelectronic Engineering, Guangdong University of Technology, Guangzhou 510006, China

ARTICLE INFO

Article history:
Received 13 June 2025
Revised 15 July 2025
Accepted 30 July 2025
Available online 30 July 2025

Keywords:
Hard carbon
Sodium-ion batteries
Biomass
Crosslinking
Anthraquinone

ABSTRACT

Biomass-derived hard carbons (HCs) have emerged as highly promising anode materials for sodium-ion batteries (SIBs), owing to their high reversible capacities as well as low cost. However, the complex internal structure of biomass precursors presents significant challenges for precise control of microstructure as well as energy storage performance of the final HC products. To address this issue, in this study, three anthraquinone (AQ)-based organic small molecules, namely AQ, 2,6-dihydroxyanthraquinone (DQ) and 2,6-diaminoanthraquinone (DAAQ), are selected as crosslinking agents of bamboo biomass, to reveal the unique role of functional groups in these molecules for the precise regulation of microstructure of the bamboo-derived HCs. The results demonstrate that, under the same aromatic carbon skeleton, hydroxyl and amino groups have significant influence on the pore structure, graphitization degree, and electrochemical performance of HCs. Among them, DAAQ with amino functional groups exhibits the best crosslinking efficiency, resulting in a more ordered carbon structure along with successful N-heteroatom doping. Consequently, the HC prepared from DAAQ-crosslinked bamboo achieves a remarkable reversible capacity of 351 mAh/g and a high initial Coulombic efficiency of 86.4% at 20 mA/g. This work demonstrates the significant potential of functionalized AQ-based molecules as efficient crosslinkers in regulating the microstructure of biomass-derived HCs.

© 2026 Published by Elsevier B.V. on behalf of Chinese Chemical Society and Institute of Materia Medica, Chinese Academy of Medical Sciences.

Sodium-ion batteries (SIBs) have emerged as a highly promising electrochemical energy storage technology in large-scale energy storage applications, owing to their low cost, high safety, and abundant sodium resources [1,2]. Among the anode materials for SIBs, biomass-derived hard carbon materials (HCs) are regarded as one of the most commercially promising candidates due to their high reversible capacity, low sodium storage potential, and low raw material costs [3,4]. However, the practical application of these materials still faces significant challenges, mainly attributed to the variability of precursor materials and the complexity of their internal structures [5]. Such factors complicate the precise control of microstructural properties during synthesis, leading to issues such as reduced initial Coulombic efficiency (ICE) and reversible capacity [6]. Therefore, effectively regulating biomass precursors to achieve precise design and optimization of the microstructure in HCs has become a critical research focus. Solving this challenge is not only essential for improving the electrochemical performance of HCs, but also provides critical technical support for promoting the commercialization of SIBs [7].

The complex biological organization and variable structure of biomass raw materials often result in carbonized products that fail to meet the requirements of high-performance electrode materials [8]. Biomass is primarily composed of cellulose, hemicellulose, and lignin, which are intricately interwoven and entangled, making it difficult to precisely control the microstructure of hard carbon during pyrolysis [9]. In recent years, researchers have proposed various modification strategies, including chemical activation, physical activation, heteroatom doping, and crosslinking, to optimize the structure of biomass precursors [10,11]. Among these approaches, the crosslinking strategy has received considerable attention because it can effectively regulate intermolecular interactions during the carbonization process. This strategy relies on organic molecules containing specific functional groups to chemically react with the functional groups present in biomass, while simultaneously introducing heteroatoms. During carbonization, a stable crosslinked network is formed, thereby optimizing the material's pore structure,

* Corresponding author.
E-mail address: yanxb3@mail.sysu.edu.cn (X. Yan).

https://doi.org/10.1016/j.cclet.2025.111651
1001-8417/© 2026 Published by Elsevier B.V. on behalf of Chinese Chemical Society and Institute of Materia Medica, Chinese Academy of Medical Sciences.

interlayer spacing, and surface chemical properties [14]. For example, Zhang *et al.* employed the dual carboxyl groups of L-aspartic acid to form stable ester bonds through esterification crosslinking reactions with hydroxyl and carboxyl groups within biomass components, thereby constructing a robust crosslinked network structure during carbonization [15]. This crosslinking strategy not only effectively prevents the structural collapse of biomass during pyrolysis, but also significantly optimizes the pore distribution and interlayer spacing of HCs. Furthermore, organic small molecules containing aromatic structures can form stable interactions with aromatic components in biomass (*e.g.*, lignin) through π-π stacking during the crosslinking process, thereby constructing a more ordered carbon skeleton structure during subsequent carbonization. For instance, Liu *et al.* systematically investigated the effects of different aromatic ring crosslinkers on the microstructure and electrochemical performance of HCs [16]. Their results demonstrated that both the number of layers and the degree of aromaticity in polycyclic aromatic resins significantly increased with the number of rings in the precursor molecules. Notably, pyrene, a four-ring aromatic compound, exhibited the highest number of aromatic layers and the strongest π-π interactions, effectively regulated the thickness of graphite layers and the size of graphite microcrystals during oxidative crosslinking, thereby optimizing the electrochemical performance of the resulting material. Although researchers have achieved significant advancements in modifying biomass precursors to control the microstructure, pore distribution, and graphite microcrystals of HCs, precisely regulating these materials remain a major challenge due to the inherent complexity of biomass's microstructure. Additionally, the reversible capacity and ICE of HCs still need further improvement [14,17].

To address the challenge of precise microstructure regulation in biomass-derived HCs, this study proposes a crosslinking strategy based on functionalized organic small molecules. By introducing specific functional groups to modify the biomass precursor, the reversible capacity and ICE of HCs are significantly enhanced. Specifically, bamboo-based biomass is first treated with hydrochloric acid. This treatment not only effectively removes inorganic salts and impurities, but also disrupts the hydrogen bonds within cellulose molecules, thereby achieving depolymerization of the biomass components and laying the foundation for subsequent precursor modification. Anthraquinone (AQ)-based organic small molecules are chosen as ideal crosslinking candidates due to their unique aromatic ring structure and tunable functional groups. Among the anthraquinone-based organic small molecules, three different types of organic molecules, namely anthraquinone, hydroxyanthraquinone and aminoanthraquinone, were selected as crosslinking agents. Compared with anthraquinone, hydroxyanthraquinone and aminoanthraquinone respectively contain two pairs of active functional groups. Among them, the amino group in DAAQ has a lower electronegativity, and its lone pair of electrons is more likely to participate in nucleophilic addition reactions; while the hydroxyl group in DQ has a higher electronegativity of the oxygen atom, which leads to an enhanced hydrogen bond effect and thus a relatively weaker crosslinking ability. Through ball milling, these molecules are uniformly dispersed within bamboo powder, and the mechanical shear force generated during the process disrupts the hierarchical structure of biomass components, providing the favorable conditions for efficient crosslinking between anthraquinone molecules and biomass. Meanwhile, the crosslinking interactions among functional groups can precisely regulate the microstructure of biomass-derived HCs, markedly enhancing its sodium storage performance. Additionally, the incorporation of functional groups enables efficient nitrogen doping, further optimizing the electrochemical performance of the HCs. Experimental results demonstrate that the developed HCs anode exhibits excellent performance, with an ICE as high as 86.4% and a reversible specific capacity of 351 mAh/g at a current density of 20 mA/g. By combining the crosslinking strategy with heteroatom doping, this study provides novel insights for optimizing the microstructure of biomass-derived HCs.

The preparation process of HCs is shown in Fig. 1a. First, the raw bamboo is crushed and sieved through a 1000-mesh sieve to obtain uniformly sized bamboo powder. The powder is then stirred in a 1 mol/L HCl solution at room temperature for 24 h to effectively remove inorganic impurities. After the reaction, the powder is repeatedly washed with deionized water until neutral. Subsequently, AQ, DQ and DAAQ are ball-milled to prepare three different precursor powders. Finally, the precursor powders are sintered at 1500 °C to successfully prepare the desired hard carbon material.

To deeply investigate the structural changes of anthraquinone-type organic molecules during ball milling, systematic characterization analyses are conducted. As shown in Figs. 1b-d, Fourier transform infrared (FTIR) spectra is performed on the ball-milled samples. The results show that B-AQ, B-DQ, and B-DAAQ samples exhibit distinct characteristic peaks at 1450, 1334, 1284, and 1167 cm^{-1}, which are attributed to the skeletal stretching vibrations of aromatic rings, confirming that the carbon skeleton of anthraquinone-type organic small molecules remains intact during ball milling without any structural damage [18]. Notably, the B-DQ sample shows a characteristic peak at 3290 cm^{-1}, corresponding to the hydroxyl disubstituted group, which matches the structural features of the DQ molecule. Additionally, the B-DAAQ sample exhibits a double peak at 3400 cm^{-1}, consistent with the characteristic absorption peak of the amino group in the DAAQ molecule. These findings fully demonstrate that ball milling changes the physical form of the samples but does not damage the carbon skeleton structure of anthraquinone-type organic molecules, providing a reliable structural basis for subsequent material preparation [19].

The pyrolysis behavior of bamboo-based biomass and anthraquinone-type organic molecule precursors were further studied by using thermogravimetric analysis (TGA). The three samples exhibited markedly distinct pyrolysis characteristics. In Fig. 1e, pure AQ demonstrated rapid weight loss between 200 °C and 250 °C, followed by complete sublimation above 300 °C, corresponding to the sublimation behavior of AQ [20]. In contrast, the B-AQ sample showed a similar rapid weight loss (66.1% mass fraction) in the same temperature range, attributed to the sublimation of AQ from the mixture. Subsequently, a relatively gradual weight loss occurred between 160 °C and 380 °C, stabilizing after 400 °C with a residual mass fraction of 4.7% for B-AQ. The calculated carbon yield from B-AQ is 7.4%, slightly lower than the residual mass fraction of pure bamboo (8.8%). Fig. 1f illustrates the pyrolysis behavior of DQ, showing rapid weight loss between 270 °C and 400 °C, stabilizing thereafter, with a final residual mass fraction of 4.8%, indicating that DQ undergoes a self-cross-linking reaction during pyrolysis. B-DQ and bamboo exhibit comparable pyrolysis behaviors, with final residual mass fractions of 9.1% and 8.8%, respectively, further confirming the correlation between their pyrolysis characteristics. In Fig. 1g, DAAQ shows a higher sublimation temperature, with rapid weight loss occurring between 300 °C and 420 °C. In contrast, B-DAAQ show rapid weight loss between 230 °C and 380 °C, with B-DAAQ having a final residual mass fraction of 27.1% [21]. Moreover, as clearly demonstrated in Figs. S1a-c, significant differences in thermal stability were observed among the derivatives at 800 °C. While AQ completely sublimated and condensed throughout the tube opening due to its low thermal stability, only minimal amounts of DQ and DAAQ were generated, indicating their superior thermal resistance and effective crosslinking with the biomass matrix. This result indicates that DAAQ undergoes cross-linking reactions with cellulose, hemicellulose, and lignin in bamboo-based biomass

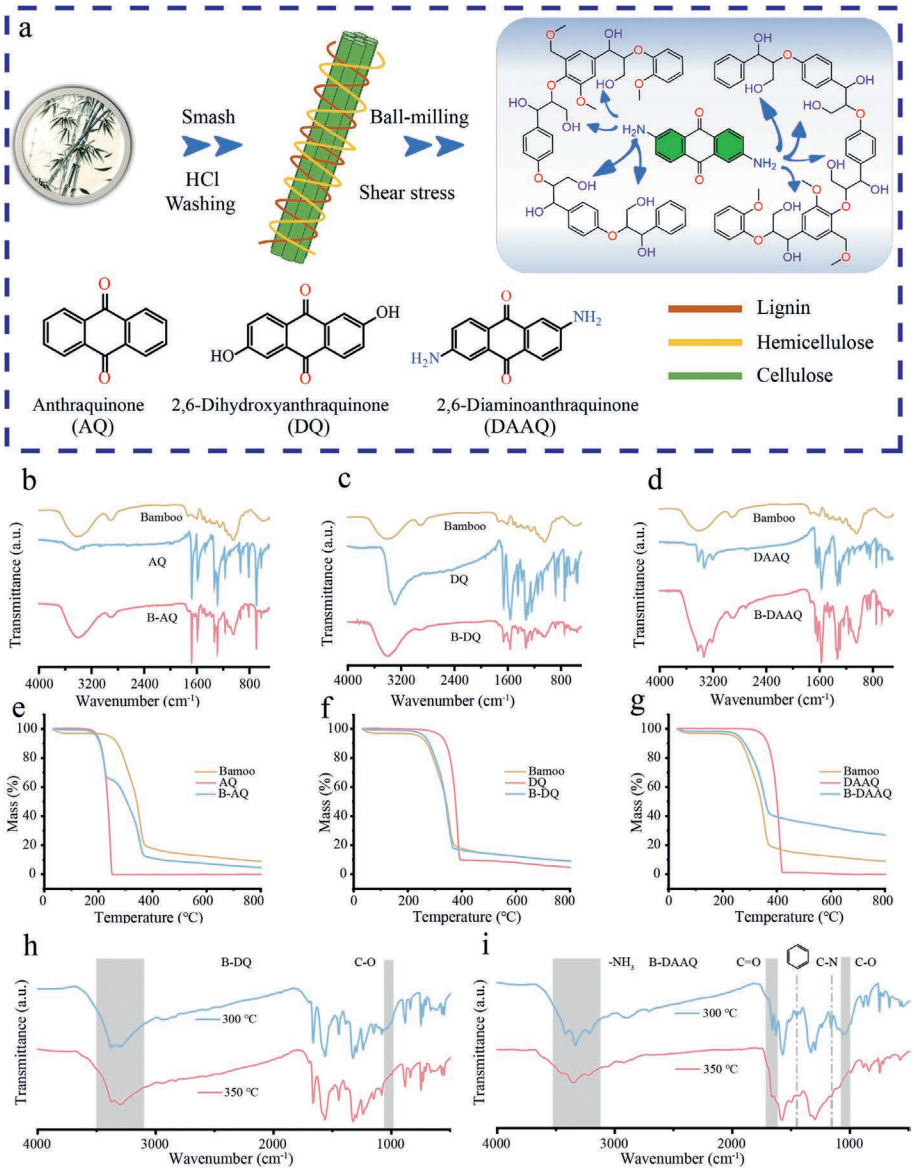


Fig. 1. (a) Schematic illustration of the synthesis procedure. (b-d) The FT-IR spectra and (e-g) TG curves of the samples. (h, i) FT-IR spectra of B-DQ and B-DAAQ at 300 and 350 °C.

during pyrolysis, which not only enhances the structural stability of the material but also effectively increases the carbon yield [22].

Considering that the weight loss behavior of B-DQ and B-DAAQ mainly occurs between 300–400 °C, FTIR is performed on samples within this temperature range. As shown in Fig. 1h, compared to B-DQ-300, the broad peak at 1030 cm^{-1} in B-DQ-350 completely disappears, which is attributed to the C–O stretching vibration of primary alcohols in cellulose and hemicellulose. This phenomenon indicates that the more active hydroxyl groups in bamboo undergo cross-linking reactions with DQ molecules, forming new chemical bonds. Similarly, in Fig. 1i, the B-DAAQ-350 sample also shows significant structural changes. Specifically, the C=O characteristic peaks at 1637 and 1660 cm^{-1} completely disappear, while the intensity of the amino peak at 3335 cm^{-1} markedly decreases. Furthermore, the characteristic peaks corresponding to the aromatic ring, C–N bonds, and C–O bonds of DAAQ, observed at 1450, 1154, and 1065 cm^{-1}, respectively, also disappeared accordingly. These changes indicate that the amino groups in DAAQ molecules undergo dehydration condensation reactions with functional groups in bamboo-based biomass, and further molecular cross-linking within the biomass is achieved through the carbon skeleton of DAAQ. This cross-linking process not only enhances the structural stability of the material but also provides a favorable chemical environment for subsequent carbonization [23].

The specific surface area (BET) of the samples is investigated using nitrogen adsorption-desorption isotherms. The isotherms reveal that all samples exhibit typical Type I and Type II adsorption behaviors, accompanied by H4-type hysteresis loops, indicating that the prepared carbon materials have significant nanoporous structural characteristics (Fig. 2a) [24]. Specifically, the BET specific surface areas of HC-B, HC-AQ, HC-DQ, and HC-DAAQ are 4.32, 3.14, 3.22, and 6.29 m^2/g, respectively. The relatively low specific surface area indicates that the material has fewer surface openings, effectively preventing solvent molecules from penetrating into the interior of HC particles through these openings, thereby reducing irreversible side reactions. Such structural characteristic not only contribute to enhancing the reversible capacity of the material but also markedly improve the initial Coulombic efficiency.

X-ray diffraction (XRD) analysis reveals the structural characteristics of the samples (Fig. 2b). The characteristic diffraction

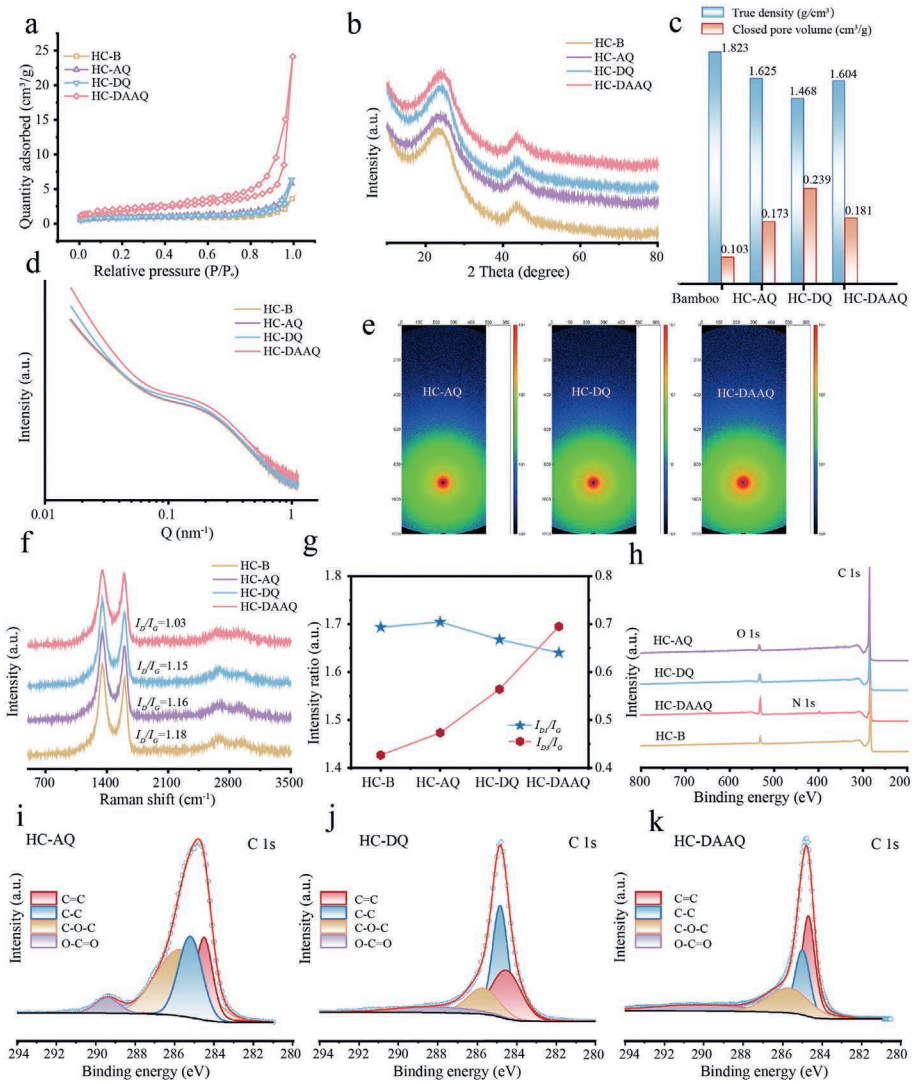


Fig. 2. (a) Nitrogen adsorption-desorption isotherm curves, (b) XRD patterns, (c) True density and pore volume, (d) SAXS curves, (e) 2D-SAXS curves, (f, g) Raman spectra and corresponding variation of the value of I_{D1}/I_G and I_{D3}/I_G. (h) XPS spectra and (i-k) C 1s high-resolution XPS spectra of different samples.

peaks observed near 23.6° and 43.5° are correspond to the (002) and (100) crystal planes of the carbon material, which suggests a higher level of graphitization in the carbon structure [25]. Peak fitting of the (002) diffraction peak (Figs. S2a-d in Supporting information) reveals that it can be decomposed into two sub-peaks corresponding to highly disordered carbon and *pseudo*-graphitic domains. The result shows that the difference of interlayers' distances of the two subpeaks is trace, HC-DAAQ has the lowest proportion of highly disordered carbon (20.80 %), further confirming its optimal graphitic structure. The R-factor, defined as the ratio of background intensity A to (002) peak intensity B, is used to quantitatively evaluate the microstructure of the material. As shown in Figs. S3a-d (Supporting information), HC-DAAQ exhibit relatively high R-factor values, again verifying that anthraquinone-type organic small molecules with cross-linking effects can effectively regulate the graphitization degree of bamboo-derived hard carbon materials. Specifically, the change in the R-factor indicates that cross-linking promotes the stacking orderliness of carbon layers, reduces the content of single-layer carbon, and thus improves the electrochemical performance of the material [26].

To better explore the regulatory effect of functional groups on the nanoporous structure of HCs, the true density of the samples was accurately measured using the true density test method. Based on the theoretical characteristics of the graphite crystal structure (ideal graphite is a layered close-packed structure with a true density of 2.26 g/cm^3), the closed pore volume of the material is calculated using the following Eq. 1:

$$V_{\text{closedpores}} = (1/\rho_{\text{true}} - 1/\rho_{\text{graphite}}) \quad (1)$$

where $V_{\text{closedpores}}$ represents the closed pore volume, ρ_{true} is the true density of the sample measured by helium gas (g/cm^3), and ρ_{graphite} is the theoretical density of ideal graphite. This test method can accurately characterize the closed pore structure in HCs that are impermeable to helium molecules. By comparing the test results of samples modified with different functional groups, the regulatory effect of these functional groups on the nanoporous structure of the material can be systematically assessed [27].

The test results (Fig. 2c) indicate that the true densities of the samples are as follows: HC-B (1.823 g/cm^3), HC-AQ (1.625 g/cm^3), HC-DQ (1.468 g/cm^3), and HC-DAAQ (1.604 g/cm^3). Upon calculation, it is found that the closed pore volume of HCs significantly increases from 0.103 cm^3/g for HC-B to 0.239 cm^3/g for HC-DQ. It is worth noting that although the closed cell volume of HC-DAAQ (0.181 cm^3/g) is lower than that of HC-DQ, its true density is relatively higher. This is mainly because after the nitrogen element is

successfully doped, the nitrogen element is incorporated into the graphite lattice, changing the electronic structure and bulk density of the material, thereby leading to an increase in the true density [12].

To further explore the regulatory mechanism of organic small molecules on the microstructure of biomass HCs, small-angle X-ray scattering (SAXS) technology was used to systematically characterize the material. The SAXS test results (Fig. 2d) show that the scattering signals in the intermediate q-value range mainly originate from the micropore structure in hard carbon materials, while the scattering signals in the low q-value range reflect the pore structure characteristics of larger scales such as mesopores and macropores [28]. Specifically, the HC-DQ sample exhibits the widest scattering platform in the SAXS spectrum, indicating that it has the highest total pore volume, followed by the HC-DAAQ sample. These closed pore structures mainly originate from the distortion and folding of sp^2 graphite layers to form nanoscale pores, a feature observed in all four hard carbon materials. At the same time, it is highly consistent with the SAXS-2D spectrum results in Fig. 2e. From the pattern brightness and intensity differences of the samples, it can be clearly seen that the HC-DQ sample exhibits the strongest scattering signal, further confirming its unique pore structure characteristics. These SAXS test results reveal that anthraquinone-type organic small molecules have a significant regulatory effect on the pore structure of biomass hard carbon [29].

Raman spectroscopy analysis serves as a critical tool for characterizing the structural orderliness of carbon materials. As shown in Fig. 2f, the Raman spectra of HC-B, HC-AQ, HC-DQ, and HC-DAAQ reveal. Characteristic peaks at 1346 cm^{-1} (D band) and 1598 cm^{-1} (G band), corresponding to structural defects and graphitic crystallinity, respectively. Generally, the area ratio of the D band to the G band (I_D/I_G) is used to quantify the graphitization degree of carbon materials [19]. The analysis shows that as the cross-linking degree increases, the I_D/I_G ratio significantly decreases from 1.18 for HC-B to 1.03 for HC-DAAQ, indicating a gradual improvement in the graphitization degree of the material. In particular, the lowest I_D/I_G value of HC-DAAQ (1.03) confirms that its optimal structural orderliness and the fewest defects, which is highly consistent with the high-resolution transmission electron microscopy (HRTEM) and XRD characterization data. In order to further analyze the structural characteristics of the material, the Raman spectra were fitted using Gaussian sub-peaks (including four sub-peaks). At 1340 cm^{-1}, the D1 band is represented as the disordered lattice vibration originated from the edge of the graphite plane. 1516 cm^{-1} is the D3 band corresponding to the amorphous carbon bonded by sp^2. 1200 cm^{-1} belongs to the D4 band and is represented as the sp^2-sp^3 hybrid structure. 1589 cm^{-1} is the G band representing the vibration mode of the ideal graphite lattice [30]. Among them, the I_{D1}/I_G ratio can characterize the graphitization degree of the material, while the I_{D3}/I_G ratio reflects the relative content of sp^2-bonded amorphous carbon and graphitic microcrystals (Fig. 2g and Figs. S4a-d in Supporting information). The analysis results show that HC-DAAQ exhibits a higher sp^2/sp^3 hybrid carbon bond ratio, which is closely related to its excellent electrochemical performance.

X-ray photoelectron spectroscopy (XPS) was further used to study the chemical composition and chemical state of HCs. As shown in Fig. 2h, the XPS full spectrum analysis shows that the HCs is mainly composed of carbon and oxygen elements, with characteristic peaks observed at 285 and 533 eV corresponding to the C 1s and O 1s orbitals, respectively. Notably, an obvious characteristic peak appears at 397 eV in the XPS spectrum of the HC-DAAQ sample, confirming the incorporation of nitrogen [13]. This result indicates that nitrogen can be effectively retained in the final product during the cross-linking process of DAAQ and bamboo-based biomass. The successful doping of nitrogen has a dual optimization effect on material performance: (1) Structural effect: The introduction of nitrogen atoms creates abundant structural defects in the carbon matrix, which can effectively improve the electrochemical activity of the material; (2) Functional effect: Nitrogen doping provides additional active sites for sodium ion storage, significantly enhancing the energy storage performance of the material. These XPS analysis results confirm the successful doping of nitrogen into the material [10].

By analyzing the high-resolution XPS spectra of C 1s (Figs. 2i-k), the characteristic peaks at 284.5 and 284.9 eV correspond to C–C and C=C bonds, respectively [22]. The analysis shows that the sp^2 carbon content significantly increases from 38.3 % for HC-AQ to 53.3 % for HC-DAAQ, which is mainly attributed to the cross-linked network structure formed by anthraquinone-type organic small molecules within the bamboo-based biomass [31]. This result is highly consistent with the Raman spectroscopy test data. Additionally, a characteristic peak at 285.6 eV is observed in the HC-DAAQ sample, which is resolved as C–N/C–O bonds, further confirming the successful doping of nitrogen. To further explore the cross-linking mechanism of DAAQ, XPS characterization was performed on the HC-DAAQ-800 sample. Through N 1s spectrum analysis (Figs. S5a and b), the N 1s spectrum of HC-DAAQ-800 can be decomposed into four characteristic peaks: 398 eV (pyridinic-N), 400 eV (amino-N), 401 eV (pyrrolic-N), and 403 eV (graphitic-N), with pyridinic nitrogen and pyrrolic nitrogen being the main forms. Notably, compared to HC-DAAQ-800, the form of nitrogen in HC-DAAQ has significantly changed (the nitrogen content decreased from 3.32 % to 1.98 %), from mainly pyridinic nitrogen and pyrrolic nitrogen to mainly amino nitrogen. This transformation indicates that during high-temperature carbonization, some nitrogen atoms escape from the graphite lattice, leading to the formation of closed pore structures. These closed pores provide ideal active sites for sodium ion storage, thereby significantly improving the reversible capacity of the material [18].

Scanning electron microscopy (SEM) and high-resolution transmission electron microscopy (HRTEM) were used to characterize the microstructure and morphological features of the products. As shown in Figs. S6a-d, SEM images show that HC-B and HC-AQ samples retain the tubular structure of bamboo fibers, while HC-DQ and HC-DAAQ exhibit sheet-like structures and short fiber morphologies. This transformation in morphology is attributed to the cross-linking effect induced by organic small molecules. By further observing the microstructure of the material through HRTEM (Figs. 3a-c), that the HC-AQ sample contains twisted graphite structures and closed pore structures. However, due to the limited availability of highly active cross-linkable functional groups in AQ molecules, their cross-linking interaction with bamboo-based biomass is limited [32]. In contrast, the HC-DQ and HC-DAAQ samples exhibit long and curved graphitic microcrystalline structures, which mainly benefit from the effective cross-linking of active functional groups within DQ and DAAQ molecules. Notably, the interlayer spacing (d_{002}) of the material significantly increases from 0.353 nm for HC-AQ to 0.418 nm for HC-DQ and 0.422 nm for HC-DAAQ. This expansion of interlayer spacing enhances the rapid transport of sodium ions, thereby improving the electrochemical performance of the material. These findings are highly consistent with the XRD and Raman test results, further confirming the regulatory effect of organic small molecule cross-linking on material structure [33].

Based on systematic characterization analysis results, Fig. 3d shows the microstructure evolution mechanism of HCs prepared from bamboo-based biomass precursors regulated by anthraquinone-type organic small molecule cross-linking. Natural bamboo-based materials are mainly composed of lignin, cellulose, and hemicellulose [13]. During pyrolysis carbonization, these components undergo significant chemical transformations, result-

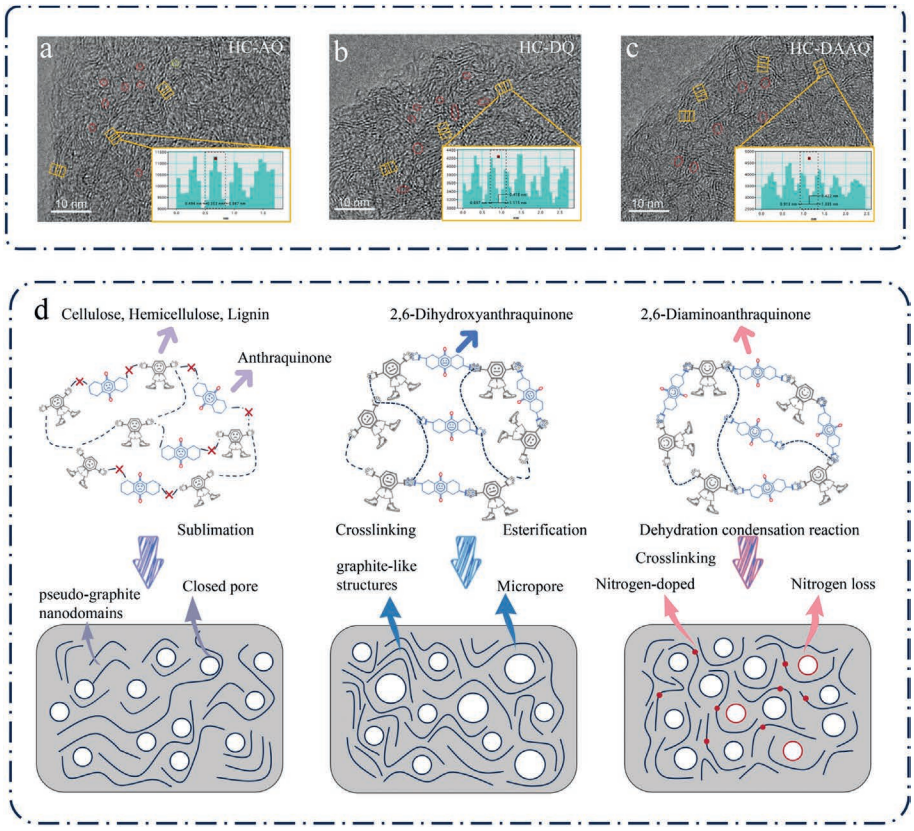


Fig. 3. (a-c) HRTEM images of the samples. (d) Schematic illustration of the structural evolution during the carbonization process.

ing in HCs with relatively low initial coulombic efficiency and reversible capacity [34]. By incorporating anthraquinone-type organic small molecules into the biomass precursor, a cross-linked network structure can be formed during carbonization, which effectively prevents the excessive dispersion of *pseudo*-graphitic domains during high-temperature carbonization, thereby avoiding the formation of open pore structures. Specifically, AQ molecules lack active functional groups and are difficult to effectively cross-link with bamboo-based biomass. In contrast, the hydroxyl and amino groups in DQ and DAAQ molecules can undergo dehydration condensation reactions with hydroxyl, carboxyl, and other functional groups in bamboo-based biomass, thereby achieving precise regulation of the microstructure of HCs. The amino groups in DAAQ molecules serve dual optimization purposes: (1) Structural enhancement: nitrogen atoms incorporate into the graphite lattice, creating additional active sites for sodium ion storage/adsorption; (2) Functional improvement: during high-temperature carbonization, partial nitrogen escape generates vacancies that provide ideal storage spaces for sodium ion filling in closed pores.

To evaluate the electrochemical performance of the prepared HCs, systematic tests were conducted in sodium half-cells within a voltage range of 0.01–3 V. As shown in Figs. 4a-c, cyclic voltammetry (CV) tests were performed on HCs at a scan rate of 0.1 mV/s. The sharp reduction/oxidation peaks observed in the 0.01–0.1 V range correspond to the plateau capacity, indicating that reversible filling/deintercalation of sodium ions between carbon layers. The weak reduction peak observed near 0.6 V can be attributed to the formation of the solid electrolyte interface (SEI) film, which is a typical feature of electrolyte decomposition during the first cycle. Notably, from the second cycle onwards, the CV curves of all samples almost completely overlap, confirming that the high reversibility of electrochemical reaction between sodium ions and carbon layers [35].

As shown in Fig. 4d, constant current charge-discharge tests were conducted at a current density of 20 mA/g, and the reversible capacities of HC-B, HC-AQ, HC-DQ, and HC-DAAQ were measured to be 325.0, 333.4, 292.6, and 351.7 mAh/g, respectively. Notably, HC-DQ exhibits the highest initial Coulombic efficiency (87.2 %), followed by HC-DAAQ (86.4 %). This performance difference is mainly due to the following two key factors: (1) Crosslinking effect: The amino groups in DAAQ molecules have stronger cross-linking ability than the hydroxyl groups in DQ molecules, enabling more effective cross-linking with internal components of biomass, thereby optimizing the material structure; (2) Doping effect: The successful doping of nitrogen in DAAQ not only improves the conductivity of the material but also provides additional active sites for sodium ion storage, significantly enhancing the reversible capacity of the material [36]. These electrochemical test results confirm that molecular design and structural regulation can effectively optimize the sodium storage performance of HCs.

As illustrated in Fig. 4e, the charge-discharge curves were analyzed to evaluate the zoned capacity. The sodium storage behavior of all electrodes can be divided into three characteristic regions: (1) High potential region (1.0–3.0 V): Corresponding to the adsorption behavior of sodium ions on the material surface, mainly occurring at surface defect sites and functional groups; (2) Slope region (0.1–1.0 V): Reflecting the intercalation behavior of sodium ions between carbon layers, which is closely related to the interlayer spacing and graphitization degree of the material; (3) Plateau region ($<$0.1 V): Attributed to the pore filling mechanism of sodium ions in closed pore structures, which contributes significantly to the overall performance of the material. As expected, HCs cross-linked with anthraquinone-type organic small molecule exhibit significantly improved plateau capacity, mainly due to the optimization of the pore structure and interlayer spacing by cross-linking, providing more active sites for sodium ion storage [37].

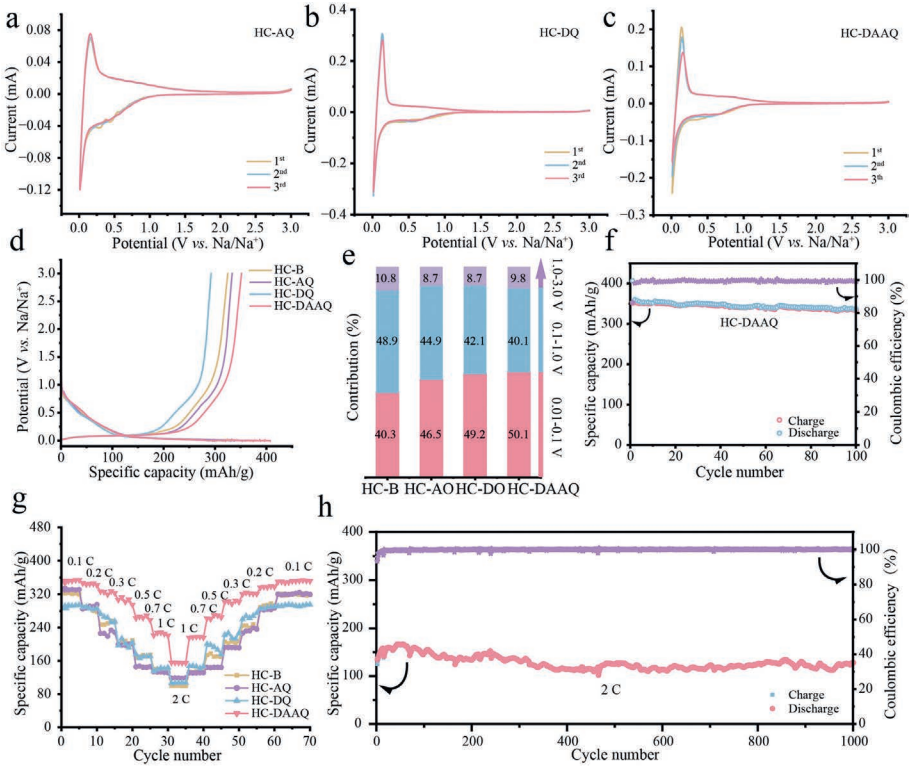


Fig. 4. (a-c) CV curve and (d) GCD curves of the samples. (e) Proportion of capacity contribution at different voltage ranges. (f) Cycling performance of HC-DAAQ at a current density of 20 mA/g. (g) Rate the performance of the samples. (h) Cycling performance of HC-BO-MA at 2 C.

Fig. 4f and Figs. S7a-c (Supporting information) show the cycle performance test results of the samples at a current density of 20 mA/g. Among them, HC-DAAQ exhibits the superior cycle stability, maintaining a reversible capacity of 334.4 mAh/g after 100 cycles, with a capacity retention rate of 95 %, while the Coulombic efficiency remains stable at 99.8 % or above. In contrast, HC-B, HC-AQ, and HC-DQ have the Coulombic efficiency retention rate of 98.9 %, 98.6 %, and 97.6 %, respectively, under the same test conditions. These data indicate that the cross-linking strategy of anthraquinone-type organic small molecules, especially the incorporation of DAAQ, significantly improves the cycle stability of HCs [38]. This performance improvement is mainly attributed three factors: Firstly, the hard carbon formed by DAAQ cross-linking has a more stable network structure, which can effectively inhibit structural degradation during cycling. Secondly, the introduced nitrogen atoms by DAAQ not only improve the conductivity of the material but also provide additional active sites, enhancing structural stability. Lastly, the optimized surface chemical properties promote the formation of a stable SEI layer, reducing the occurrence of side reactions [39].

Fig. 4g shows the rate performance test results of HC-B, HC-AQ, HC-DQ, and HC-DAAQ. As the current density gradually increases from 0.1 C to 2 C, the specific capacity of all samples shows a regular attenuation, which is mainly attributed to the transition in the sodium ion storage mechanism from pore-filling processes at low current densities to surface adsorption-dominated at high current densities [11]. Notably, when the current density is restored to 0.1 C, all samples can recover to their initial capacity values, fully confirming that the material has excellent reversibility and structural stability. Among these materials, HC-DAAQ exhibits superior rate performance, maintaining a reversible capacity of 160 mAh/g even at a high current density of 2 C. To further evaluate its cycle stability at high-rate conditions, a long-term cycling test of 1000 cycles was performed on HC-DAAQ at 2 C (Fig. 4h). The test results show that after 1000 cycles, HC-DAAQ can still maintain a reversible capacity of 128 mAh/g, and the average Coulombic efficiency remains stable at 99.8 %.

To further evaluate the optimization effect of the cross-linking strategy on electrochemical performance, CV tests were conducted on HC-AQ, HC-DQ, and HC-DAAQ at scan rates from 0.1 mV/s to 1.0 mV/s, and the results are shown in Figs. 5a-c. As the scan rate increases, the CV curves of all samples maintain good shapes, indicating that the electrodes have small polarization and excellent structural stability [40]. To analyze the kinetic characteristics of the samples, the test data were fitted using the power law equation. The relationship between peak current (i) and scan rate (v) can be described by the following equation:

$$i = av^b \tag{2}$$

$$\log i = b\log v + \log a \tag{3}$$

where i and v represent peak current and scan rate, respectively, and a and b are fitting constants. The b value, as an important kinetic parameter, has a clear physical meaning: when the b value is close to 1, it indicates that the electrode material mainly undergoes surface capacitive behavior; when the b value is close to 0.5, it reflects a diffusion-controlled Faraday process. As shown in Figs. 5d and e, the b values of all samples are between 0.5 and 1, indicating that indicating that the electrode material is influenced by a combination of both processes [41].

To further quantify the capacitive contribution and diffusion-controlled contribution of the samples, the CV curves were fitted using Eq. 4:

$$i = k_1 v + k_2 v^{1/2} \tag{4}$$

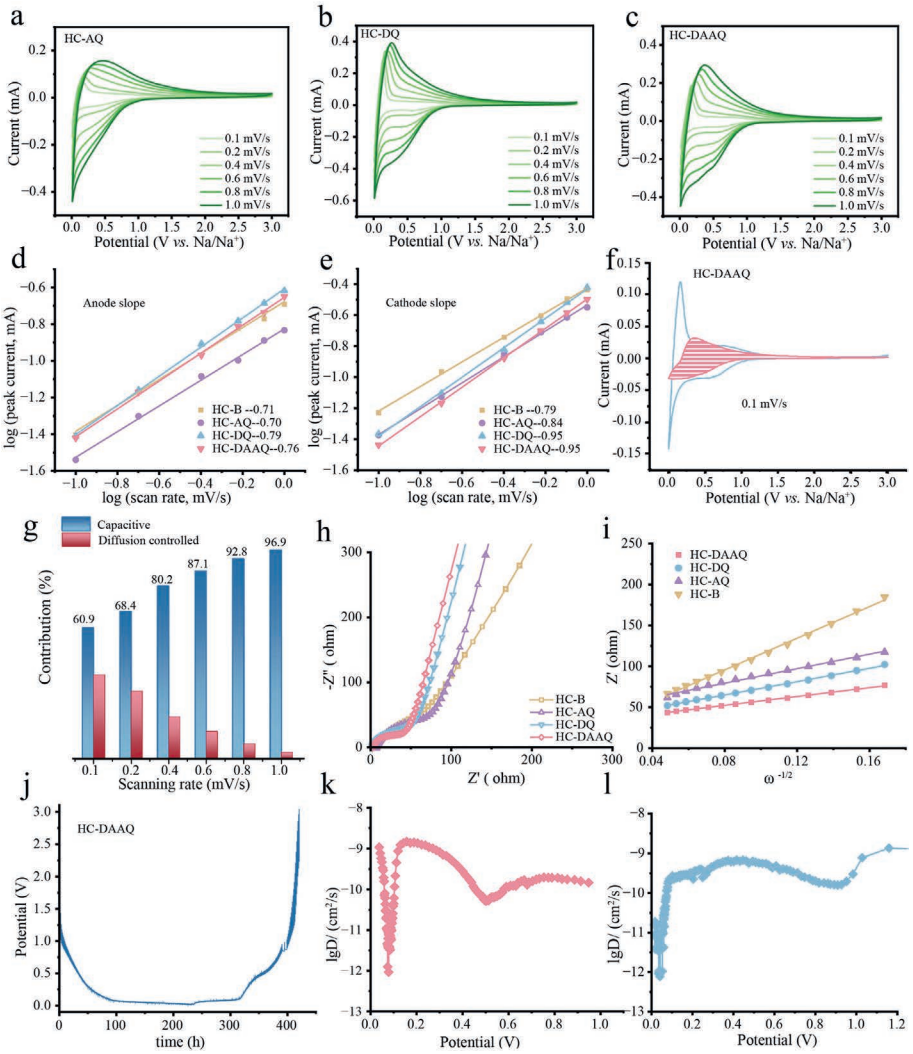


Fig. 5. (a-c) CV curves at different scan rates. (d, e) Linear relationship between log(*i*) and log(*v*). (f) CV curves displaying the capacitive contribution (red area) to the total current at 0.1 mV/s of HC-DAAQ. (g) Contribution ratios of capacitive capacity at different scan rates. (h) Nyquist plot of the sample. (i) Plots of *Z*' *versus* $\omega^{-1/2}$. (j) The GITT curve of HC-DAAQ. (k, l) The Na^+ diffusion coefficient in discharge process and charge process.

where *i* represents peak current, *v* is the scan rate, and k_1 and k_2 are fitting constants for capacitive contribution and diffusion contribution, respectively. As shown in Fig. 5f, the filled part shows the capacitive control contribution at a scan rate of 0.1 mV/s. As the scan rate increases from 0.1 mV/s to 1 mV/s, the capacitive contribution significantly increases from 60.9 % to 96.9 % (Fig. 5g). This trend indicates that at lower scan rates, the sodium ion storage process includes both capacitive behavior and diffusion-controlled behavior, where the diffusion-controlled behavior mainly originates from the intercalation/deintercalation of sodium ions between carbon layers; as the scan rate increases, the capacitive contribution gradually dominates, reflecting that at high rates, sodium ions are mainly stored through the surface adsorption mechanism. This rapid response surface capacitive behavior is key to the excellent rate performance of the material [32].

Electrochemical impedance spectroscopy (EIS) was used to systematically analyze the reaction kinetics and sodium ion diffusion coefficient of the electrode materials. Fig. 5h shows the Nyquist plots of the electrodes at room temperature. The impedance spectra of all samples exhibit typical characteristics: The semicircle in the high-frequency region corresponds to the charge transfer resistance (R_{ct}), while the linear tail in the low-frequency region reflects the Warburg diffusion impedance (*W*) [42]. The test data show that the R_{ct} values are 97.6 Ω (HC-B), 87.9 Ω (HC-AQ), 68.6 Ω (HC-DQ), and 52.9 Ω (HC-DAAQ). These findings clearly illustrates that the cross-linking strategy of anthraquinone-type organic small molecules, especially the introduction of DAAQ, significantly reduces the charge transfer resistance of the material. This optimization helps improve the reversible capacity and Coulombic efficiency of the material, which is highly consistent with the electrochemical performance test results. In addition, based on the EIS test data, the sodium ion diffusion coefficient (*D*) of the electrode material was calculated using Eq. 5:

$$D = \frac{1}{2}\left(\frac{RT}{An^2F^2C\sigma}\right)^2 \quad (5)$$

where *R*: Gas constant (8.314 J mol^{-1} K^{-1}), *T*: Absolute temperature (K), *A*: Effective surface area of the electrode (cm^2), *n*: Number of charge transfers, *F*: Faraday constant (96,485 C/mol), *C*: Bulk concentration of sodium ions (mol/cm^3), σ: Warburg coefficient, which can be determined by the linear fitting slope of the real part impedance *Z*' *versus* the square root of the angular frequency $\omega^{-1/2}$ in the low-frequency region of the Nyquist plot.

Fig. 5i shows the linear fitting relationship between *Z*' and $\omega^{-1/2}$ of the electrode materials. The analysis shows that the

Warburg coefficient σ values of HC-B, HC-AQ, HC-DQ, and HC-DAAQ are 412.04, 443.6, 407.7, and 271 $\Omega s^{-1/2}$, respectively. Among them, HC-DAAQ exhibits the smallest fitting slope, indicating that it has the best sodium ion diffusion characteristics. Based on Eq. 5, the sodium ion diffusion coefficients (D) are calculated as: HC-B (8.43×10^{-19} cm^2/s), HC-AQ (7.28×10^{-19} cm^2/s), HC-DQ (8.61×10^{-18} cm^2/s), HC-DAAQ (1.95×10^{-18} cm^2/s). This strongly confirms the significant improvement in the sodium ion diffusion kinetics of hard carbon materials by the cross-linking strategy of anthraquinone-type organic small molecules [43].

To further analyze the sodium ion diffusion kinetics of HC-DAAQ, galvanostatic intermittent titration technique (GITT) was used for systematic characterization. The sodium ion diffusion coefficient (D_{Na^+}) can be calculated according to Fick's second law, using the following Eq. 6:

$$D = \frac{4}{\pi\tau}\left(\frac{m_B V_M}{M_B S}\right)^2\left(\frac{\Delta E_S}{\Delta E_\tau}\right)^2 \quad (6)$$

In the formula, τ is the relaxation time, m_B is the mass of the active material, M_B is the molar volume of HC, V_M is the molar volume of HC, S is the electrode surface area, and ΔE_S and ΔE_τ are obtained from the GITT curve. As shown in Figs. 5j-l, the GITT test results reveal the sodium ion diffusion behavior of HC-DAAQ in different potential regions [44]. During the discharge process, a higher D_{Na^+} is observed in the slope region (1.0–0.2 V), which is mainly due to the rapid adsorption of sodium ions in open pores and surface defect sites; in the 0.2–0.1 V range, D_{Na^+} drops sharply, reflecting the saturation of available active sites, and sodium ions begin to intercalate between graphite layers; when the voltage drops below 0.1 V, D_{Na^+} rises significantly again, mainly due to the process of sodium ions filling closed pores. Correspondingly, during the charging process, D_{Na^+} shows a completely opposite trend to the discharge process, indicating that the material has excellent reversibility [35,45,46].

In this study, we developed an innovative cross-linking strategy that utilizes functionalized AQ-based organic molecules to precisely regulate the microstructure of biomass-derived HCs, significantly enhancing their electrochemical performance in SIBs. By using AQ, DQ and DAAQ as cross-linking agents, we achieved efficient cross-linking of bamboo biomass and optimized the pore structure, interlayer spacing, and surface chemical properties of the prepared HCs. Among them, DAAQ, containing amino functional groups, exhibited superior cross-linking efficiency, resulting in a more ordered carbon structure and successful nitrogen doping, both of which improving electrical conductivity and providing additional sodium ion storage sites. Consequently, the HC-DAAQ demonstrated outstanding performance, with a reversible capacity of 351.7 mAh/g and an ICE of 86.4%. This work highlights the potential of functionalized anthraquinone molecules as effective cross-linking agents for tailoring the microstructure of HCs, and contributes to the development of biomass-derived HCs for sustainable and cost-effective SIBs.

CRediT authorship contribution statement

Yandong Xie: Writing – review & editing, Writing – original draft. **Sishi Li:** Validation. **Shiyin Xie:** Methodology. **Yulong Zhang:** Investigation. **Ziqiang Fan:** Data curation. **Yuecong Chen:** Formal analysis. **Jian Zhu:** Data curation. **Qingyun Dou:** Validation. **Xingbin Yan:** Funding acquisition.

Declaration of competing interest

The authors declare that they have no known competing financial interests or personal relationships.

Acknowledgments

This work was financially supported by the National Key R&D Program of China (No. 2022YFB2402600), the National Natural Science Foundation of China (No. 52203346), the Guangdong Basic and Applied Basic Research Foundation (Nos. 2022B1515120019, 2021A1515110168). We thank Dr. Jingying Sun (Instrumental Analysis and Research Center, Sun Yat-sen University) for assistance with TEM measurements.

Supplementary materials

Supplementary material associated with this article can be found, in the online version, at doi:10.1016/j.cclet.2025.111651.

References

[1] F. Wang, T. Zhang, T. Zhang, et al., Nano-Micro Lett. 16 (2024) 148–194.
[2] L. Xie, C. Tang, Z. Bi, et al., Adv. Energy Mater. 11 (2021) 2101650.
[3] J. Cui, P. Su, W. Li, et al., Adv. Energy Mater. 15 (2025) 2404604.
[4] Y. Yang, C. Wu, X.X. He, et al., Adv. Funct. Mater. 34 (2023) 2302277.
[5] E.I. Akpan, B. Wetzel, K. Friedrich, Green Chem. 23 (2021) 2198–2232.
[6] Y. Wan, Y. Liu, D. Chao, et al., Nano Mater. Sci. 5 (2023) 189–201.
[7] C. Matei Ghimbeu, A. Beda, B. Réty, et al., Adv. Energy Mater. 14 (2024) 2303833.
[8] H. Wang, H. Chen, C. Chen, et al., Chin. Chem. Lett. 34 (2023) 107465.
[9] M. Thompson, Q. Xia, Z. Hu, et al., Adv. Mater. 2 (2021) 5881–5905.
[10] M.X. Song, L.J. Xie, J.Y. Cheng, et al., J. Energy Chem. 66 (2022) 448–458.
[11] L. Wang, Z. Xu, P. Lin, et al., Adv. Energy Mater. 15 (2024) 2403084.
[12] Y. Sun, T. Shen, H. Pan, et al., Appl. Surf. Sci. 680 (2025) 161422–161431.
[13] T. Zhang, T. Zhang, F. Wang, et al., J. Energy Chem. 96 (2024) 472–482.
[14] A. Wang, G. Zhang, M. Li, et al., Prog. Mater. Sci. 152 (2025) 101452–101508.
[15] Y. Zhang, Z. Zhou, Q. Lin, et al., Chem. Eng. J. 515 (2025) 163768–163780.
[16] Y. Liu, H. Niu, Z. Wang, et al., Carbon 242 (2025) 120433–120444.
[17] F. Wang, Z. Jiang, Y. Zhang, et al., eScience 4 (2024) 100181–100220.
[18] Y. Xie, X. Wang, L. Hou, et al., J. Energy Storage 38 (2021) 102530–102540.
[19] Y. Wang, Z. Yi, L. Xie, et al., Adv. Mater. 36 (2024) 2401249.
[20] N. An, Z. Hu, H. Wu, et al., J. Mater. Chem. A 5 (2017) 25420–25430.
[21] H. Ma, Y. Tang, B. Tang, et al., Carbon Energy 6 (2024) 584–597.
[22] W. Yang, Y. Mo, W. Zhou, et al., Adv. Funct. Mater. 35 (2025) 2509129.
[23] J. Lin, Q. Zhou, Z. Liao, et al., Angew. Chem. Int. Ed. 63 (2024) 202409906.
[24] C. Wu, Y. Yang, Y. Zhang, et al., Angew. Chem. Int. Ed. 63 (2024) 202406889.
[25] S. You, Q. Zhang, J. Liu, et al., Energ. Environ. Sci. 17 (2024) 8189–8197.
[26] Z. Tang, R. Zhang, H. Wang, et al., Nat. Commun. 14 (2023) 6024.
[27] J. Peng, H. Wang, X. Shi, et al., Adv. Mater. 37 (2025) 2410326.
[28] T. Xu, X. Qiu, X. Zhang, et al., Chem. Eng. J. 452 (2023) 139514.
[29] Q. Hu, L. Xu, G. Liu, et al., ACS Nano 18 (2024) 21491–21503.
[30] Q. Peng, K. Wang, Y. Gong, et al., Adv. Funct. Mater. 33 (2023) 2308284.
[31] X. Feng, Y. Li, Y. Li, et al., Energ. Environ. Sci. 17 (2024) 1387–1396.
[32] K.Y. Zhang, H.H. Liu, J.M. Cao, et al., Energy Storage Mater. 73 (2024) 103839.
[33] X. Li, S. Zhang, J. Tang, et al., J. Mater. Chem. A 12 (2024) 21176–21189.
[34] T. Zhang, T. Zhang, C. Zhao, et al., Adv. Funct. Mater. 35 (2025) 2425234.
[35] J. Liu, S. Li, Y. Xie, et al., Chin. Chem. Lett. 34 (2023) 111112.
[36] Y. He, D. Liu, J. Jiao, et al., Adv. Funct. Mater. 34 (2024) 2403144.
[37] Z. Song, M. Di, X. Zhang, et al., Adv. Energy Mater. 14 (2024) 2401763.
[38] L. Bai, J. Chen, Y. Zhang, et al., Nano Energy 135 (2025) 110692.
[39] W. Ji, Z. Yi, M. Song, et al., J. Energy Chem. 94 (2024) 551–559.
[40] J. Yan, H. Li, K. Wang, et al., Adv. Energy Mater. 11 (2021) 2003911.
[41] D. Zhang, G. Chen, H. Wang, et al., Chin. Chem. Lett. 33 (2022) 3925–3930.
[42] J. Wang, L. Yan, B. Liu, et al., Chin. Chem. Lett. 34 (2023) 107526.
[43] M. Song, L. Xie, F. Su, et al., Chin. Chem. Lett. 35 (2024) 109266.
[44] Y. Mao, Z. Yi, L. Xie, et al., Energy Storage Mater. 73 (2024) 103845.
[45] X. Chen, C. Liu, Y. Fang, et al., Carbon Energy 4 (2022) 1133–1150.
[46] Z. Huang, J. Huang, L. Zhong, et al., Small 20 (2024) 2405632.